Materials Chemistry and Physics 160 (2015) 119–130

Contents lists available at ScienceDirect

Materials Chemistry and Physics

journal homepage: www.elsevier.com/locate/matchemphys

Simple synthesis of Al_2O_3 sphere composite from hybrid process with improved thermal stability for catalytic applications

Regina C.R. Santos [a, *], Antônio N. Pinheiro [b], Edson R. Leite [b], Valder N. Freire [c], Elisane Longhinotti [a], Antoninho Valentini [a]

[a] Department of Analytical Chemistry and Physical Chemistry, Federal University of Ceará, Campus of Pici, Fortaleza, CE, CEP: 60440-554, Brazil
[b] Department of Chemistry, Federal University of São Carlos, São Carlos, SP, CEP: 13560-905, Brazil
[c] Department of Physics, Federal University of Ceará, Campus of Pici, Fortaleza, CE, CEP: 60440-554, Brazil

HIGHLIGHTS

- Al and Si/Al oxide spheres with promising properties are synthesized by hybrid method.
- Al_2O_3 spheres show high thermal stability and resistance the loss surface area.
- The SiO_2 addition plays an important role in the structure and porosity of the spheres.
- Al_2O_3 and SiO_2/Al_2O_3 spheres presented a good activity to conversion ethanol.
- The activity is related to the surface area and density of OH groups on surface.

GRAPHICAL ABSTRACT

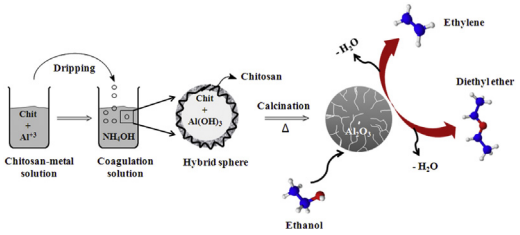

ARTICLE INFO

Article history:
Received 24 June 2014
Received in revised form
6 April 2015
Accepted 9 April 2015
Available online 11 April 2015

Keywords:
Oxides
Heat treatment
Sintering
Surface properties

ABSTRACT

Aluminium oxide spheres were synthesized by the hybrid process applying the biopolymer chitosan. After the calcination process the porous spheres were characterized by Chemical elemental analysis (XRF), X-ray diffraction (XRD), Scanning electron microscopy and Energy Dispersive X-ray Spectroscopy (SEM-EDS), N_2 adsorption–desorption isotherms, infrared spectroscopy (IR), and CO_2 temperature programmed desorption (CO_2-TPD). The effect of thermal treatment on surface properties of the oxide spheres was also evaluated by the catalytic ethanol dehydration reaction. The hybrid method produced interesting results related to the thermal stability against sintering process and consequently low decreases of surface area. The hybrid spheres calcination at 900 and 1200 °C produced a metastable phases of alumina with a high surface area, and nanometric crystallites. Additionally, the spheres of mixed silica-alumina synthesized by this method reveal the formation of porous spheres with highly acidic OH groups, which was suggested by the catalytic performance.

1. Introduction

Metastable forms of aluminium oxide, the so called transition alumina are used as adsorbents, coatings, as catalyst or catalyst support material [1,2]. Thus, the performance of alumina in its

* Corresponding author.
E-mail address: reginaclaudiasantos@yahoo.com.br (R.C.R. Santos).

http://dx.doi.org/10.1016/j.matchemphys.2015.04.014
0254-0584/

applications could be optimized by adjusting the surface area, pore structure and morphology [3,4]. However, when these materials are applied for high temperature catalytic process (above 800 °C), the advantage of high surface area and porosity is lost due to the sintering and phase transformation to thermodynamically stable α-alumina phase [1,4].

In order to prepare a stable porous and high surface area alumina, several synthetic routes have been reported. Among the methods could be cited: the precipitation [5], the sol–gel [6] and the hydrothermal [7]. Each of the various methods proposed has its advantages, but also its drawbacks. For instance, the relatively high price of alkoxy aluminium as the alumina source and organic surfactants as the structure directing agents are less attractive for practical applications. Therefore, many attempts have been made to retard the sintering process and the consequently surface area decrease. These challenges of the transition alumina oxides may be carried out by controlling the morphology during the synthesis process [8–10].

Recently, a versatile and simple method for the preparation of porous metal oxide spheres was reported [11]. This process makes use of biopolymer chitosan as directing agent of porous and spherical form. Previous works concerning this method [11,12], were restricted to the synthesis process and morphology of the composites. Thus, it is still a challenge to detail the thermal resistance of the samples synthesized by this synthesis route.

With the aim of contribute to the study of the method, herein is shown the synthesis of metastable transition aluminium oxide and mixed aluminium and silicon oxide spheres. However, higher attention was devoted to the pure aluminium oxide spheres. Thus, the mixed silica-alumina spheres were calcined at 600 °C and, the samples composed of aluminium oxide were calcined in the range of 300 °C–1300 °C. This range of temperature was adopted with the aim of to investigate the thermal resistance against the lowering surface area and porous volume. The effect of thermal treatment on the properties of the oxide spheres was evaluated by the XRD, N_2 adsorption–desorption isotherms, FTIR, SEM-EDS and CO_2-TPD. Additionally, the catalytic dehydration of ethanol was used as a model reaction in order to evaluate the acid–base properties of the samples synthesized.

Table 1
Elemental chemical composition determined by XRF on the solids, given in mass %. Nominal Si/Al molar ratio = 1.

Samples	Percentage of elements (wt.%)				
	Al	Si	Ca	Fe	Cl
Chitosan	0.00	18.09	66.76	8.94	2.12
Al300[b]	88.97	3.14	4.78	1.11	0.35
Al500	96.55	0.12	2.16	0.86	0.00
Al700	96.23	0.14	2.77	0.71	0.00
Al900	95.46	0.71	2.90	0.82	0.00
Al1200	95.01	0.70	2.95	0.97	0.00
Al1300	95.90	0.50	2.42	0.87	0.00
SiAl[a]	47.15	46.60	4.35	1.42	0.00

[a] Si/Al molar ratio = 0.95.
[b] 29.9 wt.% of residual carbon, determined by TG.

2. Experimental

2.1. Materials

Chitosan with high deacetylation degree (94%) was used as polymeric template. Aluminium nitrate nonahydrate [$Al(NO_3)_3 \cdot 9H_2O$], ammonia solution (30%), anhydrous ethanol and tetraethylorthosilicate (TEOS), all analytical grade, were used as chemical reagents.

2.2. Synthesis and heat treatment of the hybrid spheres

Porous alumina oxides spheres were synthesized, by using biopolymer chitosan as a porosity directing agent and aluminium nitrate as aluminium source, as previously reported [11]. Initially, chitosan was dissolved in acetic acid solution (3% v/v) under continuous stirring at room temperature, in the proportion of 3 g/100 mL. After, the aluminium nitrate solution, corresponding to molar ratio of chitosan/Al^{+3} of ½, was added dropwise into the chitosan solution under stirring. The resultant mixture of chitosan-metal was pumped and dripped into an alkaline NH_4OH solution 15% v/v (500 mL of solution with monitoring the pH in the range of 9–11). This procedure resulted in formation of gel spheres by precipitation of aluminium hydroxide simultaneously with the chitosan coagulation.

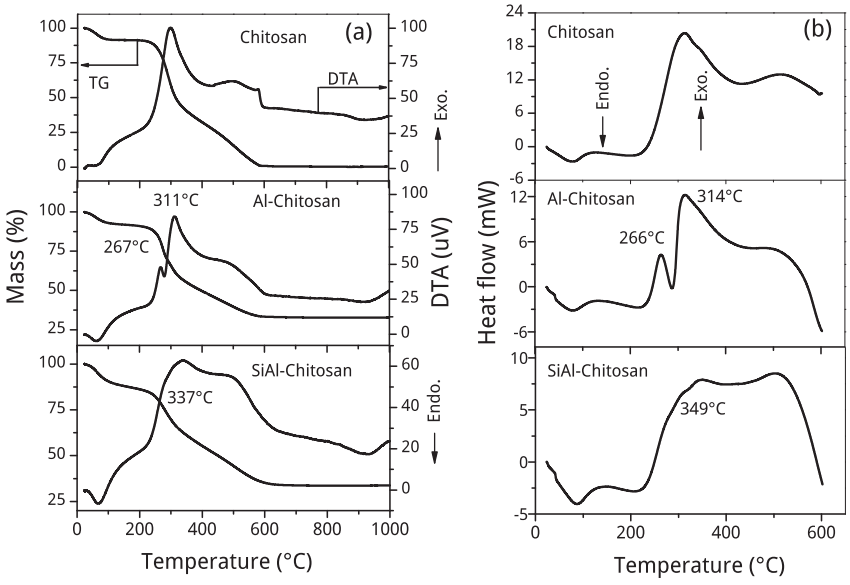

Fig. 1. Thermal analysis: (a) DTA and TGA curves and (b) DSC curve of the dried chitosan-metal spheres.

The gel spheres were then separated and dried at room temperature. Finally, the dried hybrid spheres were calcined at 300, 500, 700, 900, 1200 and 1300 °C for 2 h under air flow with a heating rate of 5 °C/min. The samples of spherical metal oxides obtained were denominated by Al300, Al500, Al700, Al900, Al1200 and Al1300. For comparison a sample containing Si and Al (nominal molar ratio = 1) was synthesized using the same procedure and calcined at 600 °C under air flow for 2 h, which was denominated by SiAl.

2.3. Characterization of oxide spheres

Thermal decomposition of the organic directing agent (chitosan in this case) was monitored by thermogravimetric and differential thermal analysis (TGA/DTA) conducted in a Shimadzu DTA-TG 60H instrument under a synthetic air flow of 40 mL/min at a heating rate of 10 °C/min. This procedure showed the various decomposition events occurring during the heat treatment of the hybrid spheres. Differential scanning calorimetry (DSC) was also performed under air flow and a heating rate of 10 °C/min.

Energy dispersive X-ray fluorescence (XRF) was performed on an X-ray fluorescence spectrometer (model ZSX mini II - Rigaku, operating conditions of 40 kV and 1.2 mA with Pd X-ray tube), for semiquantitative analysis of elements with atomic mass greater than or equal to that of fluorine.

To identify the phases and crystalline changes due to the calcination process, X-ray diffraction (XRD) data were collected with a Rigaku diffractometer using Cu Kα radiation source (λ = 1.5405 Å), and 2θ from 10° to 90°. Using the software X-Pert HighScore (Panalytical) the different transition alumina has been identified and the crystallography data for all phases were obtained using the Inorganic Crystal Structure Database (ICSD). Crystalline structure refinements were performed via the Rietveld method [13] employing the software DBWS-9807a [14] through the graphical interface DBWSTools [15]. This is designed for structural parameters refinement through a least squares method, which minimizes the difference between experimental with a calculated model patterns. The Pseudo-Voigt function was used to calculate the diffraction peaks profiles. The minimization was carried out by observing the evolution of the index parameters R_{WP} (weighted residual error) and the value of the quality factor Goodness of fit (S_{GoF}) close to 1, which confirms the good quality of the refinement [16].

Table 2
The structural models (ICSD Database) of all alumina phases used for the Rietveld refinement.

Crystalline phase	Space group	ICSD code	Reference
Eta-alumina (η)	Fd3m	66558	[24]
Gamma-alumina (γ)	Fd3m	66559	[24]
Gamma-alumina (γ)	I41/amd	99836	[25]
Theta-alumina (θ)	C2/m	82504	[26]
Alpha- alumina (α)	R-3c	9772	[27]

In order to assist in analysing the evolution of the phases, the Fourier transformed infrared (FT-IR) spectroscopy was carried out in the range of 400–4000 cm^{-1}. The FT-IR technique can provide information concerning the structural changes of various polymorphous alumina and chemical groups present on the surface.

Nitrogen adsorption–desorption isotherms were measured on a Quantachrome Autosorb-1B instrument at the temperature of liquid nitrogen. The samples were degassed at 250 °C prior to the measurement. The specific surface area of the samples was calculated using the BET method. The pore size distribution was derived from the adsorption branches of the isotherms using the Barett–Joyner–Halenda (BJH) method. The t-Plot method (Harkins and Jura equation) was applied to obtain the micropore volume and area [17]. Additionally, the isotherms were also examined by NLDFT (non local density functional theory) method, in order to compare the pore size distribution (a N_2 carbon kernel file was applied).

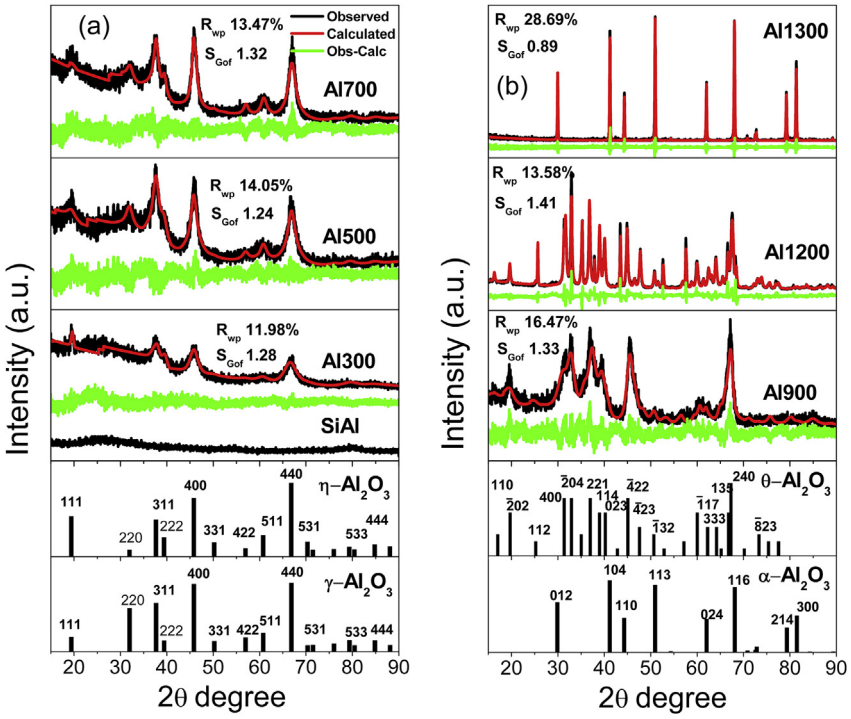

Fig. 2. Comparison between the observed and the calculated XRD patters of the alumina. The difference is shown below them. (a) aluminium oxide spheres calcined from 300 °C to 700 °C and SiAl; (b) spheres of aluminium oxide calcined from 900 °C to 1300 °C.

Table 3
Structural parameters obtained from Rietveld refinements for aluminas samples calcined at different temperature and average crystallite size.

Samples	Space group	CP[a]	Structure	Lattice parameters (Å)			V(Å^3)[b]	D(nm)[c]
				a	*b*	*c*		
Al300	Fd3m	eta η-Al_2O_3	Cubic (spinel)	7.97			506.38	3.5
Al500	Fd3m	γ-Al_2O_3	Cubic (spinel)	7.89			492.31	4.2
Al700	I41/amd	γ-Al_2O_3	Tetragonal	5.60		7.84	246.13	5.7
Al900	C2/m	θ-Al_2O_3	Monoclinic	11.97	2.82	5.59 β 103.42°	184.04	8.0
Al1200[d]	C2/m	(θ + α) -Al_2O_3	(θ) Monoclinic	11.78	2.90	5.61 β 104.01°	186.44	24.6
	R-3c		(α) Hexagonal (rhombohedral)	4.747		12.990	253.50	40.9
Al1300	R-3c	α-Al_2O_3	Hexagonal (rhombohedral)	4.759		12.992	254.91	59.9

[a] Crystalline phase.
[b] Cell volume.
[c] Average crystallite size from XRD using the Scherrer equation.
[d] Weight percentage of crystalline phase from Rietveld refinement (wt.%): 80.94(θ) +19.06 (α).

Scanning electron micrographs (SEM) were recorded using a scanning electron microscopy (FEG-SEM, Inspect F50, FEI) operating at 20.0 kV with an EDS system coupled to the SEM microscope.

The CO_2 temperature-programmed desorption experiment was performed to determine the surface basicity of various samples. Prior to TPD, the sample (0.2 g) was heat-treated at its calcination temperature for 30 min under a nitrogen flow and cooled under the same gas flow to 60 °C. The CO_2 adsorption was carried out by a flow of pure CO_2 through the reactor for 0.5 h at 40 °C. After the baseline stabilization under He flow (20 mL/min) at room temperature, the CO_2-TPD run was carried out with the heating rate of 10 °C/min from room temperature up to 500 °C. The desorbed CO_2 was detected by an online thermal conductivity detector (TCD) after passing by a trap (−20 °C) to remove traces of water. A calibration curve using known volume of CO_2 was prepared to determine the amount of CO_2 desorbed from the samples.

2.4. Dehydration of ethanol

The catalytic tests were carried out in a fixed bed flow reactor, using 0.150 g of catalyst at 250 °C. Before the reaction, the catalyst was activated under a stream of pure N_2 during 3 h at atmospheric pressure and 350 °C. A mixture containing N_2 and vapour of ethanol (at total flow of 30 mL/min), which flowed through the reactor, was established by N_2 flow through a saturation system (flask) containing ethanol at 25 °C. The mixture at the outlet of the reactor was analysed by gas chromatography equipped with a flame ionization detector (FID) and capillary column.

3. Results and discussion

The thermal behaviour of the hybrid spheres (metal -chitosan) was studied by DSC, TG and DTA techniques, and the experimental curves are shown in Fig. 1(a and b). Three main events of weight loss were observed in TGA curves for all the samples. The first endothermic weight loss, below 100 °C, is attributed to desorption of physically adsorbed water.

The DSC and DTA profile shows exothermic weight loss for the second and third events. The second weight loss in the range of 200 °C–350 °C is associated with the thermal decomposition of the chitosan [11]. However, it is interesting to notice a shift to higher temperature for this event, due to the aluminium and silicon presence. This shift may be due to the interaction between chitosan groups (OH and NH_2) with the Al^{3+} [18]. The small peak observed at 267 °C for the Al-chitosan sample, is due to the residual ammonium nitrate decomposition [19]. This exothermic decomposition can promote an additional elimination of the organic precursor and the dehydroxylation process of the material [5,19].

The SiAl-Chitosan sample also shows the exothermic event due to the ammonium nitrate decomposition, which is observed as a shoulder in the DTA and DSC curves. Therefore, for the temperature range of 200 °C–350 °C, the higher weight loss observed for Al-chitosan sample (~42.4%), regarding the SiAl-chitosan (~30.7%), is due to the higher content of nitrate. The superior amount of residual nitrate in the hybrid spheres of Al-chitosan is due to the higher content of aluminium nitrate in the precursor mixture. Fig. 1 also shows a broad exothermic peak in the temperature range of 350 °C–600 °C, which is due to the combustion process of the residual carbon and further sample dehydroxylation.

Chemical analyses of the natural biopolymer chitosan and calcined solids that were synthesized in this study are presented in Table 1. It is important to point out that the equipment used does not allow detecting the carbon; consequently the chitosan sample presented a very high weight percent (wt %) of Ca, Si and Fe.

As observed in Table 1 all the samples show the presence of Ca, Si and Fe. These compounds are impurity from chitosan, which the calcium is the main compound. The biopolymer chitosan is produced by the deacetylation of chitin, which was extracted from the exoskeletons of crustaceans (shrimp shells). Therefore, the presence of calcium carbonate, the main impurity observed, is expected [20].

On the other hand, as presented in Fig. 1, the TG of chitosan shows only 0.3 wt% of residual mass after 800 °C. Therefore, it suggests that the semiquantitative XRF analysis (Table 1), may be overestimating the amount of Ca, Si and Fe in the spheres. However, as showed previously in the literature [21–23] a low wt% content of silicon or calcium affect the alumina properties, such as the phase transition and consequently the surface area during the heat treatment.

The phase transformations of the samples due to the heat treatments from 300 to 1300 °C were followed by X-ray diffraction (XRD). The calculated intensities (Rietveld refinement), the experimental X-ray diffraction (XRD) patterns, and the difference between the experimental and calculated are shown in Fig. 2(a and b) for all alumina calcined from 300 to 1300 °C. In addition, the ICSD – PDF standard data of alumina phases are also shown as vertical bars for comparison.

As can be seen in Fig. 2, the temperature increasing in the heat treatment promotes the structural transformation of the

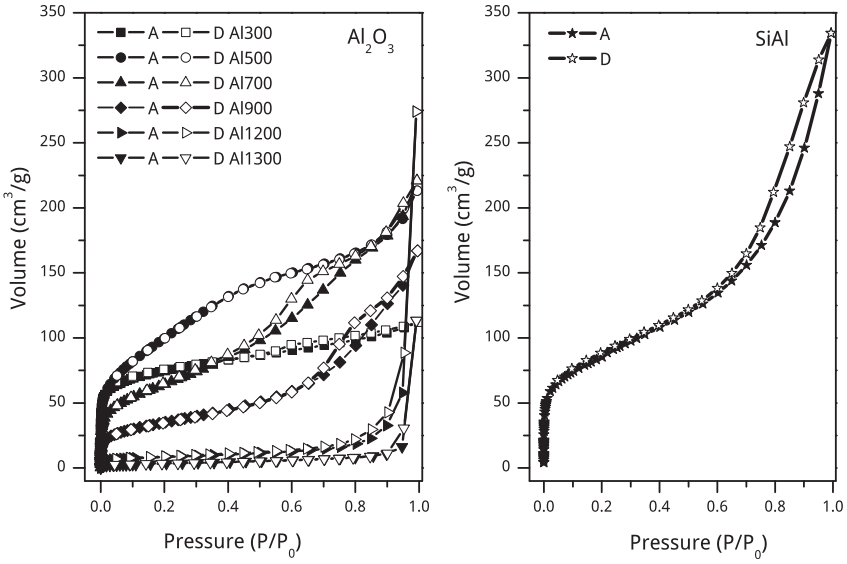

Fig. 3. Nitrogen adsorption–desorption isotherms of alumina calcined under different temperature and SiAl sample calcined at 600 °C.

aluminium oxide, forming the called transition alumina. As cited previously, in the present paper the phase transformation and structural parameters was evaluated by using the Rietveld method [13] of refinement. Rietveld refinement was performed using the structural models (ISCD database) [24–27] of all alumina phases listed in Table 2.

The main structural parameters extracted from Rietveld refinement for the various aluminium oxide phases are described in Table 3.

Fig. 2a and b shows the thermal evolution of the aluminium oxide samples synthesized, which due to the heat treatment at low temperature (300 °C) resulted in the η-Al_2O_3 phase formation (ICSD 66558). After thermal treatment at 500 °C it transform to γ-Al_2O_3 phase (ICSD 66559). Both present in the form of the conventional cubic spinel structure with Fd3m symmetry (Table 3). Therefore, there is a high structural similarity between these two phases in the XRD pattern. The γ- and η-alumina phases have a spinel cubic structure with the lattice parameter a, b and c of, 0.789 and 0.797 nm, respectively. This low contraction of the unitary cell is confirmed by the similar value of the cell volume (Table 3). Hence, a method to distinguish each other is to evaluate the relative intensities of the 400 and 440 reflections peaks, which are different for η-phase and are of approximately equal for γ-phase [28]. Furthermore, the intensity of the 220 reflection peak (at ca. 2θ of 31.9°), is very weak for the η-phase; whereas, this reflection peak is more significant for the γ-phase (Fig. 2a).

The XRD patterns suggest that the γ-Al_2O_3 phase remains stable up to 700 °C; nevertheless, it has changed to a tetragonal symmetry (ICSD 99836). The two unit cells (cubic and tetragonal) models were tested to fit of the sample heat treated at 700 °C. Both models resulted in a satisfactory refinement of the data, as suggest the rather low weighed agreement factors Rwp (15.9 and 13.47) and S_{GoF} (1.56 and 1.32) for the cubic and tetragonal model, respectively. However, as the tetragonal model gives a slightly better Rwp and S_{GoF}, it was considered here more adequate to correctly describe the structure of the alumina calcined at 700 °C prepared by hybrid method. The same test was considered for the Al500 sample, and it was observed the Rwp (14.05 and 17.15) and S_{GoF} (1.24 and 1.51) for the cubic and tetragonal model, respectively. Due to the weak signal intensity of the XRD the change in the XRD pattern is not enough to a visible distinction. The main difference is in the peak near 2θ of 67, for the tetragonal phase is 67.09 and for cubic phase is 66.8.

On the other hand, it is interesting to point out the differences for the cell volume between cubic and tetragonal (Table 3), this suggests that due to the heat treatment increasing from 500 to 700 °C promoted a small structure deformation. Consequently the cubic unit cell is no more adequate, changing to tetragonal, however, with a different atom number (low cell volume).

Table 4
Effects of calcination temperature and addition of silica upon the pore structure determined by N_2 adsorption–desorption isotherms.

Samples	BET surface area (m^2/g)[a]	Micropore surface area (m^2/g)[b]	Micropore volume (cm^3/g)[c]	Mesopore volume (cm^3/g)[d]	Pore volume (cm^3/g)[e]	NLDFT pore volume (cm^3/g)[f]
Al300[g]	269	169	0.050	0.123	0.173	0.138
Al500	369	148	0.027	0.302	0.329	0.234
Al700	231	12	0.003	0.340	0.342	0.223
Al900	124	–	–	–	0.258	0.124
Al1200	31	–	–	–	0.467	0.027
Al1300	13	–	–	–	0.176	0.011
SiAl	304	11	0.002	0.515	0.517	0.257

[a] N_2 Isotherm: BET area.
[b] t-Plot Method: micropore area and volume.
[c] t-Plot Method: micropore area and volume.
[d] Volume of mesopores estimated from the equation: $V_{meso} = V_{total} - V_{micro}$.
[e] Pore volume at $P/P_0 = 0.99$.
[f] Total NLDFT cumulative pore volume.
[g] 29.9 wt% of residual carbon, determined by TG.

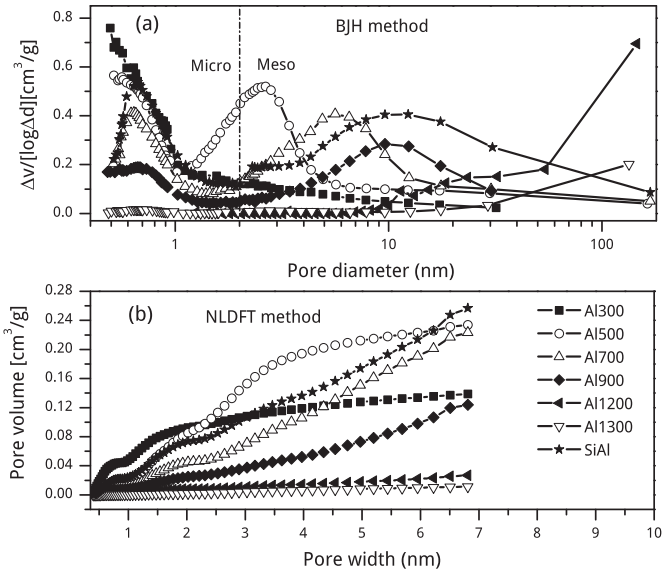

Fig. 4. Pore size distributions for samples (a) calculated using the BJH adsorption model and (b) NLDFT method presented in form of cumulative pore volume distributions from N_2 adsorption isotherms.

Inserted in Fig. 2a and b are the values calculated for the numerical criteria of fit considered (R_{wp} and S_{GoF}) for all alumina phases. The low values obtained points to the adequacy of the proposed models, which justify the procedure for structural elucidation of the alumina phases.

Differently from the Al300 or Al500, the SiAl sample showed an XRD profile of amorphous material (Fig. 2a), even after the calcination process at 600 °C. Therefore, it point out the effect of silicon oxide addition, suggesting a higher energy barrier for crystallization of alumina particles in the presence of silicon oxide [22]. The SiAl - chitosan solution dripped into the NH_4OH solution can give of Si—O—Al linkage with higher stability due to condensation of silanol groups of the silica and hydroxyl of aluminium hydroxide [29,30]. Additionally, the silicon oxide plays a role of a physical barrier, which prevents the sintering process of aluminium oxide.

With further increasing of the calcination temperature for the sample containing only aluminium oxide (Fig. 2b), it is observed a superior number of peaks and the diffraction peaks becomes sharper. Calcining at 900 °C, the θ-Al_2O_3 phase (ICSD 82504) with monoclinic crystal structure was formed; however, the presence of a small proportion of γ-Al_2O_3 cannot be ruled out. When the calcination temperature is raised to 1200 °C a mix phases can be observed, which have the θ-Al_2O_3 as the main phase and some weak peaks due to the alpha-alumina phase. The total transition of θ- Al_2O_3 to the stable α-Al_2O_3 phase (corundum, ICSD 9772) with all the characteristic diffraction peaks is observed only for the sample calcined at 1300 °C.

Although the calcination temperature increasing from 300 to 900 °C promoted the crystalline phase change from η to θ, the crystallite diameter presented a very low value, increasing from 3.5 nm (300 °C) to 8.0 nm (900 °C) (Table 3).

The average crystallite size can be estimated applying the Scherrer equation [5,31] for a specific peak, normally the main or the higher intensity. However, the values presented in Table 3 are the mean diameter considering all diffraction peaks, after Rietveld refinement, for each Al_2O_3 phases. As observed in Table 3, the crystallite size change from 3.5 to 59.9 nm with the increase in the calcinations temperature from 300 °C to 1300 °C, respectively. However, considering the temperature of 1200 °C the crystallite diameter for the α-Al_2O_3 phase is not expressive, 40.9 nm, with only 19.06 weight percent of alpha phase.

The N_2 adsorption—desorption isotherms for the samples are shown in Fig. 3 and, detailed analysis of the isotherms is summarized in Table 4.

The isotherm of the sample Al300 is characterized as type I, based on the IUPAC classification, with an inexpressive H4 hysteresis loop nearly horizontal. The adsorption process mostly happens at very low P/P_0, which is characteristic of microporous solids [1,32]. The N_2 isotherms for the samples heat treated at 500, 700 and 900 °C are of type IV (according to IUPAC classification), pointing to the presence of micro- and mesoporous [32]. However, the isotherm for the samples Al700 and Al900 shows an H4 hysteresis loop, while for the Al500 sample an inexpressive hysteresis phenomenon at higher relative pressure is observed. Therefore, the heat treatment at 500 °C promotes an increasing in the porous diameter, relatively to the Al300 sample; however, the high adsorption step at low relative pressures for the sample Al500 suggests further contain a substantial amount of microporosity.

On the other hand, the calcination process at higher temperature (Al1200 and Al1300) resulted in pronounced changes in isotherm profile. These samples present a small amount of N_2 adsorption at low relative pressure ($P/P^0 < 0.1$), and an inexpressive H3 hysteresis loop at higher relative pressures. These features of isotherms are typical from macroporous material (type III according to the IUPAC classification). Interestingly the isotherm profile for the sample SiAl is of type IV, similar to the Al500 and Al700 samples; however, it present an H3 hysteresis loop with a larger N_2 adsorption at high relative pressure.

Fig. 4 gives differential pore size distributions for the samples, calculated by the BJH method (Fig. 4a) using the adsorption branch of the isotherm and, cumulative pore volume distributions calculated from N_2 adsorption isotherms using NLDFT model (Fig. 4b).

The BJH pore size distribution shows a micro- and mesoporosity structure for the transition alumina calcined from 300 to 900 °C and SiAl sample. However, a microporosity predominance, with pore size < 2 nm, was observed in Al300 sample. An increase in the calcination temperature to 500, 700 and/or 900 °C as well as for the silica added sample (SiAl), resulted in a slight shift of pore size distribution towards mesoporosity (2—50 nm), confirming the changes suggested by the adsorption isotherms (Fig. 3). Additionally, the pore size distribution for the sample Al500 corroborates the morphology suggested by the adsorption isotherm; it is a mesoporous sample with a high ratio of microporous.

When the alumina was heat treated at 1200 and 1300 °C the majority of the pores lie in the macroporous range of >50 nm, which show the textural effect (the occurrence of sintering and grain growth) promoted by an increase in the calcination temperature.

These morphologic changes, which have occurred due to the calcinations temperature increasing, are also reflected in the application of the NLDFT method for the pore size analysis of these isotherms (Fig. 4b). The NLDFT corroborate well with the BJH pore diameter distribution, which clearly show the dependence of the pore size distribution with the calcination temperature of the samples. It is observed that the Al300 sample mostly adsorbs in the narrow micropores (pores lower than 2 nm), a microporous sample, therefore. The practically total residual carbon combustion at 500 °C (Al500 sample) resulted in elimination of a ratio of pore wall (carbon) with diameters less than 2 nm, generating an increase of the fraction of cumulative pore volume in the range of 2—7 nm, which also corroborate well with the BJH distribution. Increasing the calcination temperature (700, 900, 1200 and 1300 °C), a progressive decrease in the pore volume with width lower than 2 nm is observed, in addition to the overall decrease noted in the mesopore

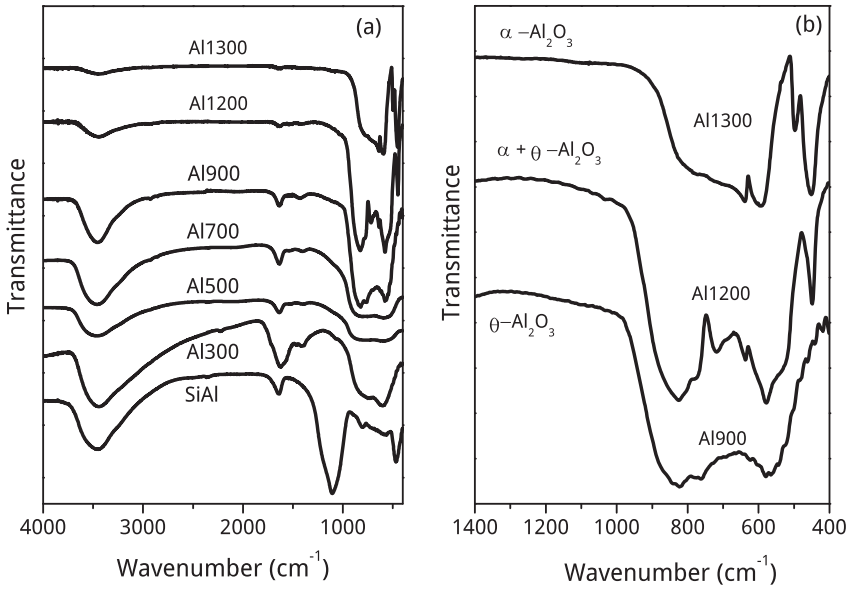

Fig. 5. (a) FTIR spectra of calcined samples and (b) magnification in the region 400–1400 cm^{-1} to samples calcined from 900 to 1300 °C.

range. Despite the pore width for the NLDFT method (Fig. 4b) be computed up to 7 nm, the total pore volume expressed in Table 4 corroborate the cumulative values expressed in Fig. 4b.

The pore volume for the sample SiAl (Table 4) is the higher value; considering the BJH pore diameter distribution this sample (SiAl) has a large fraction of pores with diameter higher than 7 nm. However, even so in the NLDFT distribution the SiAl present the higher value for the cumulative pore volume. Therefore, the data presented here point to both methods as valid for the pore size distribution analyses of samples synthesized by hybrid spheres method.

The surface area and pore volume of the samples are listed in Table 4. The γ-Al_2O_3 synthesized by the hybrid spheres process, presented in this work, produced a highest surface area value than

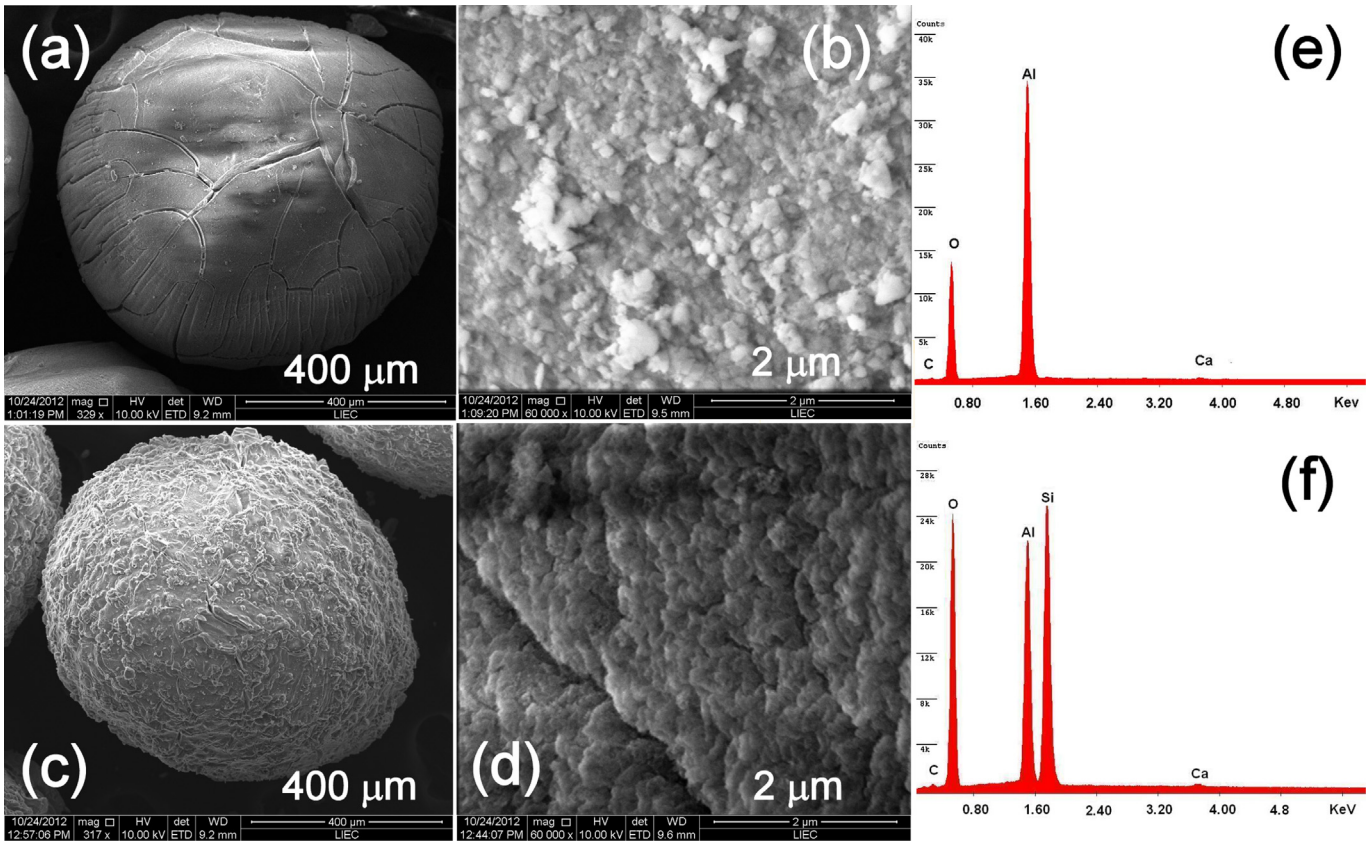

Fig. 6. SEM micrographs of (a,b) Al500 and (c,d) SiAl spheres. EDS spectrum of the samples are shown, respectively in (e) and (f).

other methods reported in the literature applying near the same calcination temperature [5,31].

Micropore surface area and volume determined using the t-plot method [1,17] shows a more pronounced microporosity in Al300 and Al500 samples. The micropore surface area for the Al300 sample represents 63% of the total surface area, whereas the Al500 sample presented 39%. This high proportion of micropore surface area for the sample Al300 is due to the residual carbon (Table 4). When the calcination temperature is increased to 500 °C the carbon is totally eliminated (Fig. 1), which results in highest BET specific surface area and mesopore volume at the expense of microporosity.

An additional increase in calcination temperature (700–1300 °C) promotes a decrease in the surface area as well as the micropore volume (Table 4). This result suggests a structural collapse with agglomeration of small particles of aluminium oxide resulting in larger mean diameter of the pores due to the sintering process. However, the transition alumina still retain a high BET surface area even after its calcination at 900 and 1200 °C (124 and 31 m^2/g, respectively), which is higher than reported by J. S. Lee et al. (25.3 m^2/g at 900 °C and 6.2 m^2/g at 1200 °C) [31], and by M.M. Martín-Ruiz et al. (9.2 m^2/g at 1200 °C) [33]. Therefore, it indicates that the alumina spheres possess a good stability against sintering process; these results corroborate the effect of preparation method [3,34]. On the other hand, the chemical composition (Table 1), suggests the Ca and Si impurities effect over the alumina stability, retarding the transition phase consequently maintaining the surface area [22,23].

Despite the difference of the time applied in the heat treatment, a comparison also may be carried out with the commercial alumina. The Versal Alumina (V-700) from UOP [35], which have a high-purity degree ($SiO_2 + Na_2O + Cl < 0.4$ wt%), present 50% of alpha phase after heat treatment at 1100 °C/1 h with a surface area of 51 m^2/g. But, after 1 h at 1260 °C is observed only the alpha phase with a surface area of 9.4 m^2/g. Another commercial alumina with purity degree in the range of 95–98 wt% is the Puralox from Sasol [36], which present ($SiO_2 + Fe_2O_3 + TiO_2$) < 0.33 wt%. The Puralox calcined at 1100 °C/24 h may present a surface area in the range of 15–80 m^2/g, and 4–40 m^2/g if calcined at 1200 °C/24 h.

The elemental composition of the samples calcined at high temperature (Table 1), represent 97 wt% of Al_2O_3, with 0.5 wt% of SiO_2 and 1.8 wt% of CaO. The presence of both, CaO and SiO_2, may contribute to the thermal stability of the sample; nevertheless, at high calcination temperature the CaO effect is no significant [23]. Therefore, these results corroborate with the data from literature [36].

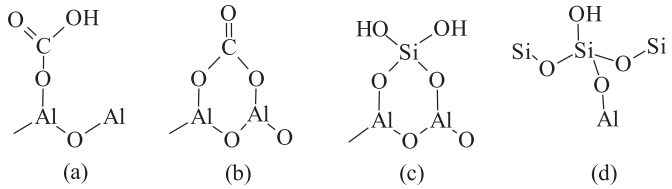

Scheme 1. (a, b) CO_2 surface species of alumina and (c, d) structure of strongly acidic silanol group with nearby Al located on the surface and in the bulk of amorphous silica-alumina [43,44].

Considering the samples calcined from 500 °C to 1300 °C, the surface area present a first order exponential decay (Table 3). Interestingly and it is important to point out that despite the composition difference the SiAl sample follows the tendency (the fit) observed for the other samples. Therefore, the presence of amorphous silica improved the pore volume; however, the calcination temperature is the main variable which affects the surface area.

Clearly, the XRD and adsorption isotherms measurements shown that the Al oxides composite spheres obtained by a hybrid spheres method is effective to prevent the transformation to α-alumina phase, and offer a high resistance for the sintering to large alumina particle. Consequently, the method is still able to maintain high surface area and porous volume, which is interesting for catalytic application process at higher temperature. This result may be attributed to decomposition of the organic (chitosan) as well as the inorganic (aluminium nitrate) precursors used (see Fig. 1), from which CO_2, NOx and H_2O were released promoting the pore formation, suppressing the crystal growth and prevent the aggregation of the alumina particles.

In agreement with the XRD patterns, the IR absorption bands of the samples appear correlating with the changes in structure. The FT-IR spectra of transition alumina spheres obtained after heating from 300 °C to 1300 °C and a mixed silica-alumina oxide calcined at 600 °C are presented in Fig. 5.

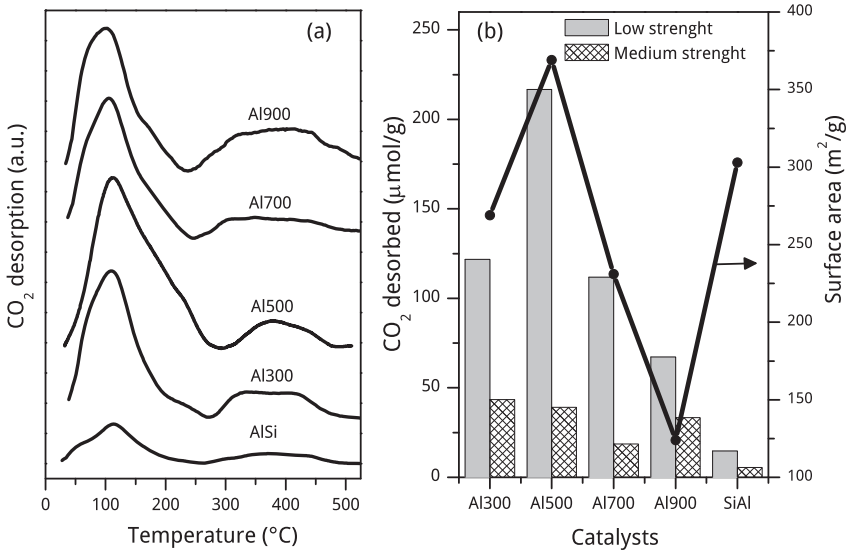

Fig. 7. (a) TPD-CO_2 profiles and (b) plot showing the correlation between amounts of CO_2 desorbed and specific surface area for calcined samples.

As observed the largest spectral changes occurred in the stretching and bending modes of the hydroxyl groups, as well as the stretching mode of the Al–O group.

Fig. 5a shows a broad and intense band around 3453 cm^{-1} and other band of medium intensity at 1628 cm^{-1} for all the samples. These are typical –OH vibrations, assigned to stretching and bending modes, respectively of adsorbed water as also to the Al–OH and Si–OH bonds [5,37]. During the heating, the intensity of these bands decrease due to dehydroxylation process but, it does not disappear completely. The weak bands observed in the range of 1530–1400 cm^{-1} in the alumina spectra is attributed to carbonate groups (CO_3^{-2}) adsorbed in the surface, which become less intense with increasing of the calcination temperature [38].

The IR spectra of aluminium oxide spheres calcined from 300 to 700 °C shows a wide unresolved band in the range of 900 cm^{-} and 500 cm^{-1}, which is assigned to Al–O stretching vibrations in AlO_6 (octahedral) and AlO_4 (tetrahedral) environments [5]. However, the increase in calcination temperature from 900 to 1200 °C or to 1300 °C improves the resolution of the spectra.

Thus, was observed a doublet in the range of 500 and 600 cm^{-1} and another in the range of 750 and 850 cm^{-1} which is assigned to stretching vibrations of both AlO_6 and AlO_4 environments, respectively [39]. This observation agrees with the XRD pattern, that suggests the formation of θ-Al_2O_3 alumina at 900 °C (Fig. 2b). For the sample calcined at 1300 °C, the FT-IR spectra shows four main vibration at 451, 498, 592 and 638 cm^{-1}, assigned to stretching of Al–O vibrations with octahedral coordination, characteristic of α-alumina phase [39]. At intermediate temperatures (1200 °C) the sample present wide vibration modes between 451 and 820 cm^{-1}, which are equivalent to the mix of θ and α-Al_2O_3 phases [39]. These results agree well with XRD observations.

The FT-IR spectra for the SiAl sample (Fig. 5a) shows a lower intensity for the bands corresponding to stretching vibrations Al–O (800 cm^{-1} and 600 cm^{-1}), and the absence of vibrations in the range of 1530–1400 cm^{-1}, which are related to the CO_3^{-2} species [38,39]. This result is due to the lower aluminium oxide content, in addition to the partial covering of aluminium oxide by the silicon oxide, which prevents the CO_2 adsorption.

The surface morphology of SiAl and Al500 samples was also examined by Scanning Electron Microscopy and Energy Dispersive X-ray Spectroscopy (SEM-EDS) (Fig. 6). The images acquired with magnification of 300 times shows a very different surface morphology of these samples. It is possible to identify the presence of fractures in the Al500 spheres (Fig. 6a) and a roughness surface for the sample SiAl (Fig. 6c) in addition to the less pronounced fractures. This surface difference may be associated with the high heat flow observed in the DTA (Fig. 1). The amount of nitrate decomposition was more meaningful for the Al500 than SiAl sample; a high energy releasing may contribute to the formation of fractures in the spheres structure. This phenomenon can also affect the formation of porous structure of the spheres.

The magnification of 60,000 times in the SEM analysis, points to a sponge feature for the sample SiAl (Fig. 6d), different of the Al500 sample (Fig. 6b). The average sphere diameter determined by SEM, after the calcination process, was 760 μm and 780 μm, for the Al500 and SiAl sample, respectively.

It is worth noticing, that in spite of the results presented in Table 1, the EDS spectrum of the samples (Fig. 6e and f) point to the presence of calcium (1.0%) for both sample, which is probably coming from the polymer used in the synthesis process (chitosan). However, unlike the result of XRF, the EDS spectrum do not suggested the presence of iron.

Fig. 7a present the CO_2-TPD curves, from which were determined the amount of the basic sites (related to the amount of CO_2 desorbed), for all the synthesized samples (Fig. 7b).

Two main desorption peaks are shown in the CO_2-TPD profiles (Fig. 7a), a peak with maximum near 110 °C and, a broad one, which extends from 250 up to 500 °C. These peaks can be assigned to the CO_2 desorbed from the basic sites with weak to moderate strengths [40]. The first peak corresponds to the formation of bicarbonates species due to the reaction of CO_2 with the surface hydroxyl groups, also acting as basic sites, the low strength site [40,41]. The second peak is associated to the interaction of CO_2 with medium strength basic sites from bidentate carbonate forms on Lewis acid–base pairs (Al^{3+}–O^{2-} pair site), which are able to desorbs CO_2 only at higher temperature [40,42].

Fig. 7b shows a direct correlation between the amounts of CO_2 desorbed from the low strength site and surface area for the Al300, Al500, Al700 and Al900 samples. Due to the heat treatment at higher temperature, the dehydroxylation process take place easier, this will result in a lower adsorption surface site (the low strength site) by surface area of sample [1,5].

Scheme 1(a,b) shows the different form of CO_2 adsorbed on sites of alumina oxide. The formation of bicarbonates may occur via the transferring of a proton from surface hydroxyl groups to the adsorbate (Scheme 1a). The carbonate species generation is possible with the simultaneous CO_2 adsorption on Lewis acid-base pair sites on surface (Scheme 1b) [43,44].

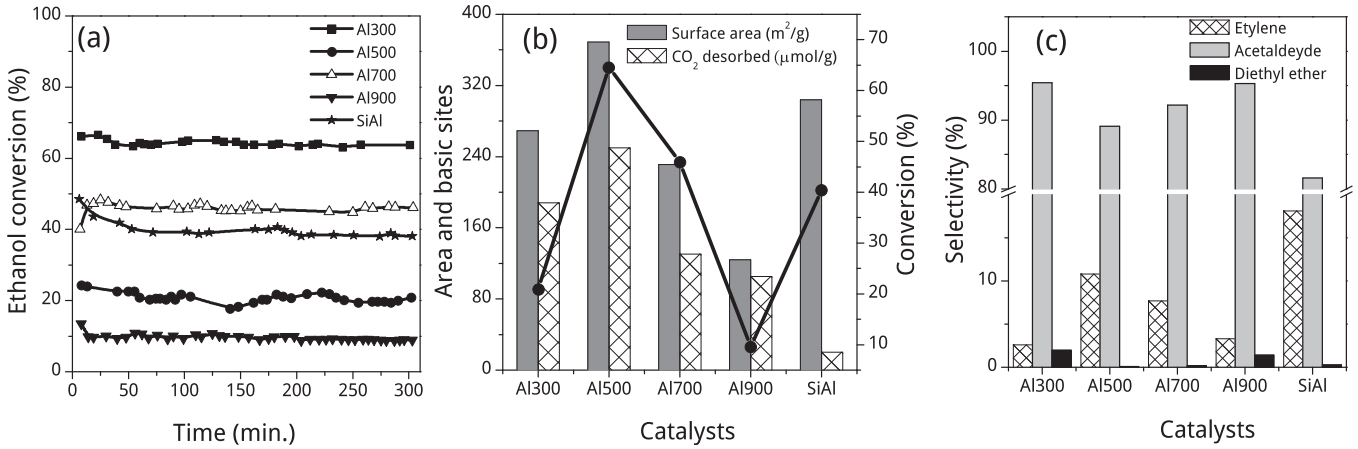

Fig. 8. Catalytic results of ethanol dehydration of oxides spheres at 250 °C: (a) Conversion in function of time, (b) Relation between surface area and amount of CO_2 desorbed with ethanol conversion and (c) product selectivity.

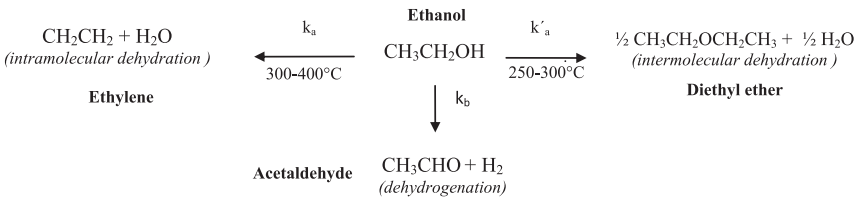

Scheme 2. Reaction scheme of ethanol conversion on acid (k_a) and basic (k_b) catalysts [46,48].

Therefore, considering the dehydroxylation process promoted by the heat treatment, the evolution of the ratio between the areas of the first event by the second event can confirm that the first event is due to the presence of bicarbonate species. So, doing the ratio between the areas of CO_2 desorbed of the first event by the second, the values obtained were 3.4, 6.5, 6.0, and 1.8 for Al300, Al500, Al700 and Al900, respectively. The low value (3.4) observed for the Al300 sample is due to the residual carbon, which leads to the presence of adsorption sites with distinct properties. However, the decreasing ratio values from 6.5 to 1.8, for the samples calcined from 500 °C to 900 °C, corroborate for the bicarbonate species in the first event of Fig. 7a. Then, as the calcination temperature increase, the dehydroxylation degree take place, favouring the formation of metal-oxygen pairs on aluminium oxide surface.

The SiAl sample, however, presented a lower value for the amount of CO_2 desorption (~20.1 μmol/g), despite the high surface area. Thus it suggests that mixed aluminium and silicon oxide possesses the most acid character on surface among the samples. It is known that the synthesis of amorphous silica–alumina (ASA) can leads to the creation of hydroxyl groups with strong Brønsted acidity located in close vicinity to an Al atom in tetrahedral environment [44]. Moreover, the strength of the acidity of the OH species of ASA could be modified both by the location of the vicinal Al atom on the surface or in the bulk. Furthermore, the distribution of various forms depends both on the preparation method and on the Si/Al ratio (Scheme 1c and d) [44].

In general this mixed silica-alumina samples are heterogeneous compounds which can contain a silica alumina mixed phase as well as alumina clusters and pure silica zones. The procedure described here, the hybrid spheres synthesis, which drips the SiAl-chitosan mixture into a NH_4OH solution, can propitiate the condensation of Si–OH with Al–OH to form Si–O–Al linkage. The heating process can promote the conversion of hexacoordinated Al into tetracoordinated Al by elimination of water as well as the decomposition of NH^{4+} into H^+ and NH_3 [30,45]. The NH_3 is desorbed and the H^+ retained on the surface increase the Brønsted acid site.

Fig. 8(a–c) shows the catalytic performance of the samples. The effect of calcination temperature over the catalytic conversion and selectivity is clear. In addition, the presence of silicon oxide (SiAl sample), also caused effect on the catalytic performance.

The alumina calcined at 500 °C (Al500), presented higher ethanol conversion, this result may be due to the highest surface area. However, the concentration of hydroxyl groups on the surface, which may act as Brønsted acid sites to activate ethanol molecule, but also as basic site (See Fig. 7), must be considered.

The literature report that ethanol conversion can be acid or base catalyzed; therefore, the product selectivity can be easily related to the acid strength of solid catalysts [46]. Ethanol is catalytically converted via two main reactions: dehydrogenation and dehydration. The intramolecular dehydration of ethanol produce ethylene, but an intermolecular dehydration may occur, which produce diethyl ether, a condensation product. At low reaction temperature diethyl ether production is favoured, while at high temperature ethylene is predominantly produced [46,47]. The main products of the catalytic conversion of ethanol are illustrated in Scheme 2. There are two pathways for product formation based on acid (k_a) or basic sites (k_b).

Indeed, the ethanol dehydration proceeds via the following steps: 1° – ethanol adsorption on the Lewis acid site; 2° – the O–H bond rupture with the participation of the basic sites, resulting in a surface ethoxy group; 3° – a second basic site can abstract a proton from the ethoxy group, which leads to a carbanion formation and finally to ethylene [48].

Considering these steps, the stronger the interaction of ethanol with the acid site, the easier the O–H bond rupture. Consequently, it should result in an easier nucleophilic attack to the abstraction of the most acidic proton in the ethoxy intermediate by the basic site and consequently giving rise to higher conversion.

Therefore, is reasonable to accept that the sample with higher amount of hydroxyl (OH) group on surface is the most active. Exactly what was observed for the catalytic conversion with the

Table 5
Comparison of conversion and selectivity upon ethanol dehydration with previously reported values.

Catalyst	Reaction conditions	Co (%)[d]	SE[e] (%)	SD[f] (%)	Ref.
Al500 (γ-Al_2O_3)	0.15 g; 250 °C[a]; WHSV 1.72 h^{-1}; 30 mL/min	64.6	10.8	89.1	This study
γ- Al_2O_3	0.5 g; 250 °C[a]; WHSV 1.43 h^{-1}; 80 mL/min	78.6	20.2	79.7	[51]
γ- Al_2O_3	0.05 g; 300 °C[a]; 1 mL/h[c]	42	25	75	[46]
SiAl600	0.15 g; 250 °C[a]; WHSV 1.72 h^{-1}; 30 mL/min[b]	40.4	18.1	81.6	This study
SiAl	0.5 g; 250 °C[a]; WHSV 1.43 h^{-1}; 80 mL/min[b]	67.5	35.1	64.9	[51]

[a] Catalyst weight.
[b] Total flow rate.
[c] Ethanol flow rate. WHSV (weight hourly space velocity).
[d] Co = conversion.
[e] SE = selectivity for ethylene.
[f] SD = selectivity for diethyl ether.

samples calcined from 500 to 900 °C. A decrease in surface area and OH site density due to dehydroxylation on surface may cause a sharp decrease in catalytic activity of the samples. The Al300 sample showed a relatively high surface area and hydroxyl group density; however, the larger presence of micropores, might have contributed to the low ethanol conversion due to diffusional limitations of the reactants and products in the catalyst pores.

Fig. 8b shows that the SiAl sample, which has high surface area, presented an ethanol conversion lower than Al500 or Al700 samples. This behaviour can be related to the lower aluminium oxide content, which leads to lower density of Lewis sites per surface area. Hence, it is interesting to point out the ethanol conversion decrease observed for the sample SiAl during the first hour (Fig. 8a), which was near 10%. This behaviour differs from the others sample, and suggest the deactivation of stronger acid site, like Brønsted acid site.

The product distribution shown in Fig. 8c revealed that the samples synthesized were mainly selective to the formation of diethyl ether and ethylene, dehydration products. It is observed the acetaldehyde presence, a dehydrogenation product, however with very low amount. The first step to ethanol conversion on metal oxide catalysts involves the adsorption of the alcohol on the surface, with formation of ethoxy intermediate. The abstraction of the hydrogen from the ethoxy group is promoted by the strong basic site on surface [48]. Thus the Al300 and Al900 with higher selectivity to acetaldehyde (2 and 1.4%) demonstrate a slightly more basic character compared to the Al500 and Al700 (<0.5% selectivity). Another factor that contributes to a higher production of diethyl ether, a condensation product, is the low temperature of the reaction (250 °C). Since the ethylene formation occurs via intramolecular dehydration, which presents highest activation energies, or requires a stronger acid site [49,50]. Therefore, the higher ethylene selectivity presented by the SiAl sample (Fig. 8c), points to the presence of strong acid sites for this sample. This result corroborates the higher rate of deactivation observed for this sample.

Accordingly, the catalytic results presented in Fig. 8(a–c), clearly points to the contribution of surface hydroxyl groups in the process. Thus, the increase in the calcination temperature, which promotes surface hydroxyl groups elimination, leads to decline in ethylene production. On the other hand, the higher strength acid of OH groups on surface lead to increase for the ethylene selectivity, as shown to SiAl sample (Fig. 8c).

Although it is possible to improve the catalytic performance by changing the reaction condition, it is interesting to make a comparison of the results presented in the literature. Other papers emphasizing the use of alumina and/or SiAl catalysts in the dehydration of ethanol have been reported. However, a comparison considering the γ- Al_2O_3 phase and the silicon oxide with aluminium oxide mixture is summarized in Table 5.

The ethanol conversion presented in the paper of T.K. Phung et al. [51] for the samples γ-Al_2O_3 and SiAl are higher, while the results observed in the paper from L. Martins et al. [46] (for the sample γ-Al_2O_3) is somewhat lower from those shown in this paper. This difference may be due to the reaction condition applied. However, the lower ethylene selectivity observed in the present paper point to inferior acid strength of the samples Al500 and SiAl. This inferior acid strength may be an effect of the calcium presence (Table 1 and Fig. 6), since the CaO is known as a basic oxide [52]. It is important to point out that it is possible to reduce the fraction of such compound (Ca or Fe), performing a chitosan purification.

On the other hand, considering the operation conditions (temperature, catalyst weight and/or lower amount of ethanol), the catalytic performance, conversion and selectivity from the present paper, are similar from those presented in the literature.

4. Conclusions

A practical methodology for the synthesis of aluminium oxide spheres with a good thermal stability was presented. This method showed promising results for the preparation of aluminium oxide with high surface area. The calcinations of the hybrid spheres at 900 and 1200 °C gave metastable phases of alumina with high surface area (124 and 31 m^2/g). The hybrid spheres synthesis route presented a high stability against changes in structural, textural and acid–base properties of the oxide phase due to the temperature heat treatment. These properties can be interesting as catalyst or catalyst support for high temperature process. The addition of silicon oxide in the sample composition promoted an increase in the strong acid sites on surface. The evolution of the changes, due to the thermal treatment, is followed efficiently by the ethanol dehydration reaction together with CO_2-TPD.

Acknowledgments

The authors acknowledge the “Federal University of Ceara”, the Brazilian research-funding support agency National Council for Scientific and Technological Development (CNPq), Dr. J.M. Sasaki (X-ray Laboratory) for the XRD measurement.

References

[1] X. Zhang, M. Honkanen, E. Levänen, T. Mäntylä, Transition alumina nanoparticles and nanorods from boehmite nanoflakes, J. Cryst. Growth 310 (2008) 3674–3679, http://dx.doi.org/10.1016/j.jcrysgro.2008.05.016.
[2] M. Arai, H. Takahashi, M. Shirai, Y. Nishiyama, T. Ebina, Effects of preparation variables on the activity of alumina-supported platinum catalysts for liquid phase cinnamaldehyde hydrogenation, Appl. Catal. A Gen. 176 (1999) 229–237, http://dx.doi.org/10.1016/S0926-860X(98)00233-6.
[3] A.I. Osman, J.K. Abu-Dahrieh, D.W. Rooney, S.A. Halawy, M.A. Mohamed, A. Abdelkader, Effect of precursor on the performance of alumina for the dehydration of methanol to dimethyl ether, Appl. Catal. B Environ. 127 (2012) 307–315, http://dx.doi.org/10.1016/j.apcatb.2012.08.033.
[4] P. Praserthdam, M. Inoue, O. Mekasuvandumrong, W. Thanakulrangsan, S. Phatanasri, Effect of organic solvents on the thermal stability of porous silica-modified alumina powders prepared via one pot solvothermal synthesis, Inorg. Chem. Commun. 3 (2000) 671–676, http://dx.doi.org/10.1016/S1387-7003(00)00165-9.
[5] H.S. Potdar, K.W. Jun, J.W. Bae, S.M. Kim, Y.J. Lee, Synthesis of nano-sized porous γ-alumina powder via a precipitation/digestion route, Appl. Catal. A Gen. 321 (2007) 109–116, http://dx.doi.org/10.1016/j.apcata.2007.01.055.
[6] A. Khaleel, S. Al-Mansouri, Meso-macroporous γ-alumina by template-free sol–gel synthesis: the effect of the solvent and acid catalyst on the microstructure and textural properties, Colloids Surf. A Physicochem. Eng. Asp. 369 (2010) 272–280, http://dx.doi.org/10.1016/j.colsurfa.2010.08.040.
[7] X. Li, T. He, M. Crego-calama, D.N. Reinhoudt, Conversion of a metastable superhydrophobic surface to an ultraphobic surface, Langmuir 24 (2008) 8008–8012, http://dx.doi.org/10.1021/la801044j.
[8] M. Akia, S. Mahdi, M. Rezaei, Z. Yan, Microporous and mesoporous materials optimizing the sol – gel parameters on the synthesis of mesostructure, Microporous Mesoporous Mater. 122 (2009) 72–78, http://dx.doi.org/10.1016/j.micromeso.2009.02.008.
[9] J.C. Ray, K.-S. You, J.-W. Ahn, W.-S. Ahn, Mesoporous alumina (I): comparison of synthesis schemes using anionic, cationic, and non-ionic surfactants, Microporous Mesoporous Mater. 100 (2007) 183–190, http://dx.doi.org/10.1016/j.micromeso.2006.10.036.
[10] C. Liu, J. Li, K. Liew, J. Zhu, M.R. Bin Nordin, An environmentally friendly method for the synthesis of nano-alumina with controllable morphologies, RSC Adv. 2 (2012) 8352, http://dx.doi.org/10.1039/c2ra20674a.
[11] T.P. Braga, E.C.C. Gomes, A.F. de Sousa, N.L.V. Carreño, E. Longhinotti, A. Valentini, Synthesis of hybrid mesoporous spheres using the chitosan as template, J. Non Cryst. Solids 355 (2009) 860–866, http://dx.doi.org/10.1016/j.jnoncrysol.2009.04.005.
[12] A. El Kadib, K. Molvinger, T. Cacciaguerra, M. Bousmina, D. Brunel, Chitosan templated synthesis of porous metal oxide microspheres with filamentary nanostructures, Microporous Mesoporous Mater. 142 (2011) 301–307, http://dx.doi.org/10.1016/j.micromeso.2010.12.012.
[13] H.M. Rietveld, A profile refinement method for nuclear and magnetic structures, J. Appl. Crystallogr. 2 (1969) 65–71, http://dx.doi.org/10.1107/S0021889869006558.
[14] C.O.P.-S.R.A. Young, A. Sakthivel, T.S. Moss Crysl, DBWS-9411 – an upgrade of the DBWS*.* programs for Rietveld refinement with PC and mainframe computers, J. Appl. Crystallogr. 28 (1995) 366–367, http://dx.doi.org/10.1107/

S0021889895002160.
[15] L. Bleicher, J.M. Sasaki, C.O. Paiva Santos, Development of a graphical interface for the Rietveld refinement program DBWS, J. Appl. Crystallogr. 33 (2000) 1189–2000, http://dx.doi.org/10.1107/S0021889800005410.
[16] A.S.B.S. Rocha, H.H.B.F.N.A. Freire, R.R. Silva, D.X. Gouveia, J.M. Sasaki, M.R.P. Santos, J.C. Góes, Structural properties study of the magneto-dielectric composite: $Cr_{0.75}Fe_{1.25}O_3$ (CRFO):$Fe_{0.5}Cu_{0.75}Ti_{0.75}O_3$(FCTO), J. Alloys Compd. 481 (2009) 438–445, http://dx.doi.org/10.1016/j.jallcom.2009.03.002.
[17] W.D. Harkins, G. Jura, Surfaces of solids. XII. An absolute method for the determination of the area of a finely divided crystalline solid, J. Am. Chem. Soc. 66 (1944) 1362–1366, http://dx.doi.org/10.1021/ja01236a047.
[18] R.B. Hernández, A.P. Franco, O.R. Yola, A. López-Delgado, J. Felcman, M.A.L. Recio, et al., Coordination study of chitosan and Fe^{3+}, J. Mol. Struct. 877 (2008) 89–99, http://dx.doi.org/10.1016/j.molstruc.2007.07.024.
[19] J. Sun, Z. Sun, Q. Wang, H. Ding, T. Wang, C. Jiang, Catalytic effects of inorganic acids on the decomposition of ammonium nitrate, J. Hazard. Mater. 127 (2005) 204–210, http://dx.doi.org/10.1016/j.jhazmat.2005.07.028.
[20] M. Rinaudo, Chitin and chitosan: properties and applications, Prog. Polym. Sci. 31 (2006) 603–632, http://dx.doi.org/10.1016/j.progpolymsci.2006.06.001.
[21] B. Beguin, E. Garbowski, M. Primet, Stabilization of alumina toward thermal sintering by silicon addition, J. Catal. 127 (1991) 595–604, http://dx.doi.org/10.1016/0021-9517(91)90185-7.
[22] K. Kosuge, A. Ogata, Effect of SiO_2 addition on thermal stability of mesoporous γ-alumina composed of nanocrystallites, Microporous Mesoporous Mater. 135 (2010) 60–66, http://dx.doi.org/10.1016/j.micromeso.2010.06.011.
[23] J.S. Church, N.W. Cant, D.L. Trimm, Stabilisation of aluminas by rare earth and alkaline earth ions, Appl. Catal. A Gen. 101 (1993) 105–116, http://dx.doi.org/10.1016/0926-860X(93)80141-C.
[24] R.S. Zhou, R.L. Snyder, Structures and transformation mechanisms of the η, γ and θ transition aluminas, Acta Crystallogr. Sect. B Struct. Sci. 47 (1991) 617–630, http://dx.doi.org/10.1107/S0108768191002719.
[25] G. Paglia, C. Buckley, a. Rohl, B. Hunter, R. Hart, J. Hanna, et al., Tetragonal structure model for boehmite-derived γ-alumina, Phys. Rev. B 68 (2003) 1–11, http://dx.doi.org/10.1103/PhysRevB.68.144110.
[26] E. Husson, Y. Repelin, Structural studies of transition aluminas. Theta alumina, Eur. J. Solid State Inorg. Chem. 33 (1996) 1223–1231.
[27] L.W. Finger, R.M. Hazen, Crystal structure and compression of ruby to 46 kbar, J. Appl. Phys. 49 (1978) 5823, http://dx.doi.org/10.1063/1.324598.
[28] J.H. Park, M.K. Lee, C.K. Rhee, W.W. Kim, Control of hydrolytic reaction of aluminum particles for aluminum oxide nanofibers, Mater. Sci. Eng. A 375–377 (2004) 1263–1268, http://dx.doi.org/10.1016/j.msea.2003.10.155.
[29] E. Finocchio, G. Busca, S. Rossini, U. Cornaro, V. Piccoli, R. Miglio, FT-IR characterization of silicated aluminas, active olefin skeletal isomerization catalysts, Catal. Today 33 (1997) 335–352, http://dx.doi.org/10.1016/S0920-5861(96)00106-X.
[30] K. Tanabe, M. Misono, Y. Ono, H. Hattori, New Solid Acids and Bases – Their Catalytic Properties, Elsevier, 1989, http://dx.doi.org/10.1016/S0167-2991(08)61046-0.
[31] J.S. Lee, H.S. Kim, N.-K. Park, T.J. Lee, M. Kang, Low temperature synthesis of α-alumina from aluminum hydroxide hydrothermally synthesized using [Al(C_2O_4)x(OH)y] complexes, Chem. Eng. J. 230 (2013) 351–360, http://dx.doi.org/10.1016/j.cej.2013.06.099.
[32] Z. Obrenović, M. Milanović, R.R. Djenadić, I. Stijepović, K.P. Giannakopoulos, M. Perušić, et al., The effect of glucose on the formation of the nanocrystalline transition alumina phases, Ceram. Int. 37 (2011) 3253–3263, http://dx.doi.org/10.1016/j.ceramint.2011.05.120.
[33] M.M. Martın-Ruiz, L.A. Pérez-Maqueda, T. Cordero, V. Balek, J. Subrt, N. Murafa, J. Pascual-Cosp, High surface area α-alumina preparation by using urban waste, Ceram. Int. 35 (2009) 2111–2117, http://dx.doi.org/10.1016/j.ceramint.2008.11.011.
[34] A.R. Keshavarz, M. Rezaei, F. Yaripour, Preparation of nanocrystalline γ-Al_2O_3 catalyst using different procedures for methanol dehydration to dimethyl ether, J. Nat. Gas. Chem. 20 (2011) 334–338, http://dx.doi.org/10.1016/S1003-9953(10)60157-0.
[35] http://www.uop.com/wp-content/uploads/2012/12/UOP-Versal-Alumina-Brochure2.pdf.
[36] http://www.sasoltechdata.com/tds/PURALOX_CATALOX.pdf.
[37] E. Barrado, J.A. Rodríguez, F. Prieto, J. Medina, Characterization of iron oxides embedded in silica gel obtained by two different methods, J. Non Cryst. Solids 351 (2005) 906–914, http://dx.doi.org/10.1016/j.jnoncrysol.2005.02.001.
[38] G. Stoica, J. Pérez-Ramírez, Reforming dawsonite by memory effect of AACH-derived aluminas, Chem. Mater. 19 (2007) 4783–4790, http://dx.doi.org/10.1021/cm071351g.
[39] A. Boumaza, L. Favaro, J. Lédion, G. Sattonnay, J.B. Brubach, P. Berthet, et al., Transition alumina phases induced by heat treatment of boehmite: an X-ray diffraction and infrared spectroscopy study, J. Solid State Chem. 182 (2009) 1171–1176, http://dx.doi.org/10.1016/j.jssc.2009.02.006.
[40] T. Montanari, L. Castoldi, L. Lietti, G. Busca, Basic catalysis and catalysis assisted by basicity: FT-IR and TPD characterization of potassium-doped alumina, Appl. Catal. A Gen. 400 (2011) 61–69, http://dx.doi.org/10.1016/j.apcata.2011.04.016.
[41] D. Yin, L. Qin, J. Liu, C. Li, Y. Jin, Gold nanoparticles deposited on mesoporous alumina for epoxidation of styrene: effects of the surface basicity of the supports, J. Mol. Catal. A Chem. 240 (2005) 40–48, http://dx.doi.org/10.1016/j.molcata.2005.06.044.
[42] J. Ni, L. Chen, J. Lin, S. Kawi, Carbon deposition on borated alumina supported nano-sized Ni catalysts for dry reforming of CH_4, Nano Energy 1 (2012) 674–686, http://dx.doi.org/10.1016/j.nanoen.2012.07.011.
[43] N.D. Parkyns, The surface properties of metal oxides. Part II. An infrared study of the adsorption of carbon dioxide on γ-alumina, J. Chem. Soc. A (1969) 410–417, http://dx.doi.org/10.1039/J19690000410.
[44] G. Crépeau, V. Montouillout, a. Vimont, L. Mariey, T. Cseri, F. Maugé, Nature, structure and strength of the acidic sites of amorphous silica alumina: an IR and NMR study, J. Phys. Chem. B 110 (2006) 15172–15185, http://dx.doi.org/10.1021/jp062252d.
[45] V.V. Boldyrev, Thermal decomposition of ammonium perchlorate, Thermochim. Acta 443 (2006) 1–36, http://dx.doi.org/10.1016/j.tca.2005.11.038.
[46] L. Martins, D. Cardoso, P. Hammer, T. Garetto, S.H. Pulcinelli, C.V. Santilli, Efficiency of ethanol conversion induced by controlled modification of pore structure and acidic properties of alumina catalysts, Appl. Catal. A Gen. 398 (2011) 59–65, http://dx.doi.org/10.1016/j.apcata.2011.03.014.
[47] H.A. Dabbagh, M. Zamani, Catalytic conversion of alcohols over alumina–zirconia mixed oxides: reactivity and selectivity, Appl. Catal. A Gen. 404 (2011) 141–148, http://dx.doi.org/10.1016/j.apcata.2011.07.024.
[48] J.I. Di Cosimo, V.K. Dıez, M. Xu, E. Iglesia, C.R. Apesteguıa, Structure and surface and catalytic properties of Mg-Al basic oxides, J. Catal. 178 (1998) 499–510, http://dx.doi.org/10.1006/jcat.1998.2161.
[49] X. Zhang, R. Wang, X. Yang, F. Zhang, Comparison of four catalysts in the catalytic dehydration of ethanol to ethylene, Microporous Mesoporous Mater. 116 (2008) 210–215, http://dx.doi.org/10.1016/j.micromeso.2008.04.004.
[50] C. de las Pozas, R. Lopez-Cordero, J.A. Gonzalez-Morales, N. Travieso, R. Roque-Malherbe, Effect of pore diameter and acid strength in ethanol dehydration on molecular sieves, J. Mol. Catal. 83 (1993) 145–156, http://dx.doi.org/10.1016/0304-5102(93)87015-Z.
[51] T.K. Phung, A. Lagazzo, M.Á. Rivero Crespo, V. Sánchez Escribano, G. Busca, A study of commercial transition aluminas and of their catalytic activity in the dehydration of ethanol, J. Catal. 311 (2014) 102–113, http://dx.doi.org/10.1016/j.jcat.2013.11.010.
[52] R.C.R. Santos, R.B. Vieira, A. Valentini, Optimization study in biodiesel production via response surface methodology using Dolomite as a heterogeneous catalyst, J. Catal. 2014 (2014) 1–11. http://dx.doi.org/10.1155/2014/213607.